Time-of-Flight Mass Spectrographs – From Ions to Neutral Atoms

E. Möbius, A.B. Galvin, L.M. Kistler, H. Kucharek, and M.A. Popecki

Space Science Center and Department of Physics, University of New Hampshire, Durham, NH

Corresponding author: Eberhard Möbius (eberhard.moebius@unh.edu)

Key Points:

- Review of time-of-flight mass spectrographs
- Versatile application of time-of-flight spectrographs for ions and neutral atoms
- Simultaneous determination of velocity distribution and composition

Abstract

After their introduction to space physics in the mid 1980's time-of-flight (TOF) spectrographs have become a main staple in space borne mass spectrometry. They have largely replaced magnetic spectrometers, except when extremely high mass resolution is required to identify complex molecules, for example in the vicinity of comets or in planetary atmospheres. In combination with electrostatic analyzers and often solid state detectors, TOF spectrographs have become key instruments to diagnose space plasma velocity distributions, mass and ionic charge composition. With a variety of implementation schemes that also include isochronous electric field configurations, TOF spectrographs can respond to diverse science requirements. This includes a wide range in mass resolution to allow the separation of medium heavy isotopes or to simply provide distributions of the major species, such as H, He, and O, to obtain information on source tracers or mass fluxes. With a top hat analyzer at the front end, or in combination with deflectors for 3-axis stabilized spacecraft, the distribution function of ions can be obtained with good time resolution. Most recently, the reach of TOF ion mass spectrographs has been extended to include energetic neutral atoms. After selecting the arrival direction with mechanical collimation, followed by conversion to ions, adapted TOF sensors form a new branch of the spectrograph family tree. We review the requirements, challenges, and implementation schemes for ion and neutral atom spectrographs, including potential directions for the future, while largely avoiding overlap with complementary contributions in this special issue.

1. Introduction

The measurement of particle populations in space, electrically charged and neutral alike, is undertaken to provide essential information toward several key objectives that are behind typical heliophysics missions, such as:

- Origin or source population of locally detected particles
- Heating of plasmas and neutral gases
- Transport and interaction of charged and neutral particles
- Acceleration of charged particles to high energies

For the evaluation of particle populations to address these questions it is essential to determine all parameters that characterize each individual particle and then to synthesize the observable distributions separately for all these parameters. The relevant key observables for particles are:

- Elemental and sometimes isotopic composition, or particle mass A
- Charge state composition, or the Ionic Charge Q of the particle
- Particle speed v, as well as arrival direction θ and ϕ

Subdivided into small increments in speed and angle, the particle count rate accumulated over pre-defined time intervals can be turned into the velocity distribution function $f(v, \theta, \Phi, t)$, including its variation over time t, for ions, electrons, and neutral atoms, separate for individual species. In this paper, we will concentrate on ion and neutral atom distributions. We will treat atoms as particles with charge state $Q = 0$. For a plasma physicist, the velocity distribution function f is the key to physical processes that control the interaction in plasmas. Instead of observing directly the particle velocity, particle sensors usually return the kinetic particle energy E along with the arrival direction. The energy E is linked to the speed v with the particle mass A, or species. With the geometric factor G the observable particle count rate can be translated into the differential particle flux $\Delta J(E, \theta, \Phi, t)/\Delta E \Delta \Omega$, which is related to the distribution function via:

$$\frac{\Delta J\left(E,\theta,\Phi,\ t\right)}{\Delta E\,\Delta\Omega}=\frac{v^2}{Am_p}f\left(v,\theta,\Phi,\ t\right) \qquad [1]$$

where $\Delta\Omega$ is the field-of-view (FoV) and ΔE the energy resolution of the sensor. By integration over a small phase space volume a particle detector obtains the count rate R in a selected angular sector with center angles θ and ϕ and at a selected center energy E, according to:

$$R(\theta,\phi,E,t)=\frac{\Delta J\left(E,\theta,\Phi,\ t\right)}{\Delta E\,\Delta\Omega}\cdot G\cdot\Delta E\,\Delta\Omega \qquad (2)$$

The situation is depicted schematically in Figure 1.

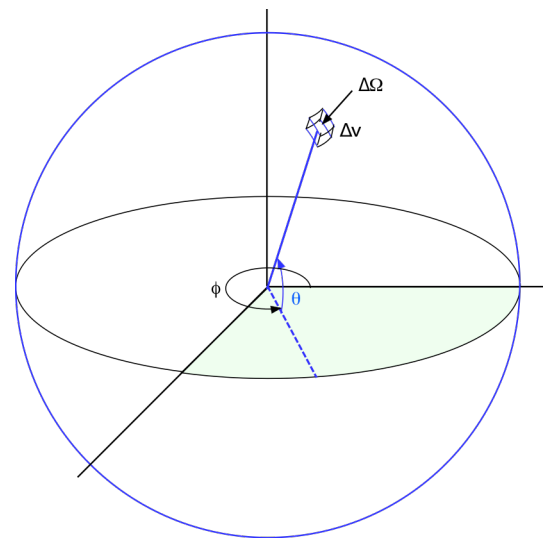

Fig. 1: Schematic view of a particle velocity distribution function $f(v,\ \theta,\ \phi)$ and how a particle detector system selects a certain portion as differential particle flux $\Delta J/\Delta E\Delta\Omega$.

Any particle counting sensor with energy resolution and a constrained FoV that is either a sub-division of a larger FoV or can be swept across the sky provides the crucial differential particle flux. However, to distinguish and thus accumulate separately particle species according to M and Q, requires additional diagnostics. In the early days of space exploration, the combination of electrostatic and magnetic deflection was employed [e.g. Coplan et al., 1978; Shelley et al., 1978] to provide mass resolution for bulk plasmas up to about 10 keV/Q. This technique is still very important for very high mass resolution in connection with in-situ sampling of planetary, lunar, and cometary atmosphere environments [e.g. Balsiger et al., 2007]. For energetic particle populations, such as solar, anomalous, and galactic cosmic rays, particle telescopes are used that obtain the energy loss ΔE in a thin detector and measure the residual energy E_R in a thick detector, where the particles are stopped, to obtain species resolution. These telescopes make use of the nuclear charge Z and mass A dependent specific energy loss in bulk material. When including gas proportional counters as ΔE elements [Hovestadt & Vollmer 1971; Hovestadt et al., 1978], this technique covers energies down to <100 keV/nucleon. The two aforementioned methods still left a substantial gap in energy coverage, in particular in the crucial suprathermal regime where ions are accelerated out of their source populations, until the arrival of time-of-flight (TOF) mass spectrographs in the 1980's [Gloeckler & Hsieh 1979; Gloeckler 1990]. Wüest [1997] provided a review in the first symposium on space plasma instrumentation.

In this paper, we will give a current overview of TOF mass spectrometry for ion and neutral atom populations with simultaneous diagnostics of their distribution functions. It is largely based on a presentation at the conference on Measurement Techniques in Solar and Space Physics and avoids substantial overlap with concurrent presentations by Gilbert, McFadden, Paschalidis, and Zurbuchen on TOF spectrometry and by Barabash and Funsten on neutral atom imaging. Where related sensors are addressed in papers for this special issue, they are cross-referenced in the appropriate Section. Section 2 will provide a brief introduction to the TOF method, its strengths and challenges. TOF spectrographs for suprathermal and energetic particle

populations will be covered in Section 3, those for thermal plasma populations and the solar wind in Section 4, high-resolution mass spectrographs in Section 5, and neutral atom imagers with mass resolution in Section 6. Section 7 contains a brief summary and indicates where TOF spectrographs may be key in the near future.

2. Brief Introduction to the Time-of-Flight Method

Compared with simple particle detectors that typically count single signals and thus are vulnerable to any noise or background count, a TOF detector, by means of its method, is a genuine coincidence detection system, which provides intrinsic noise and background suppression. As the name implies, for each incoming particle the measurement of the flight time τ between a start and a stop detector across a known distance d is obtained, which requires two independent detections of the same particle. Two generic TOF configurations are shown in Figure 2. The start signal is obtained in most cases from the passage of a thin foil, typically made of carbon, where the particle generates secondary electrons. These are accelerated and steered to an electron multiplying detector (channeltron or micro-channel plate, MCP) by means of appropriate electrostatic field configurations. The stop signal may be detected directly or, again, through secondary electrons. In the left panel of Figure 2, the electrons from the start and stop location are accelerated toward the center of the sensor, cross each other, and are deflected by a transverse field to a start and stop MCP at each end. In the right panel a configuration with electrostatic mirrors is shown, which reflect the start and stop electrons to start and stop MCP at opposite sides of the sensor perpendicular to the particle trajectory. While the former configuration contains fewer grids that reduce the sensor transparency and generate more scattered particles, the latter configuration allows to obtain the start and stop position in two dimensions from the signals. The choice depends on the measurement requirements.

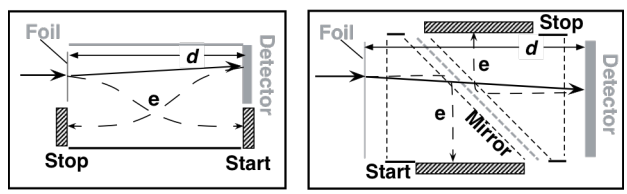

Fig. 2: Schematic view of generic TOF sensors. Particles enter through a thin C-foil from the left and traverse the TOF path d to a detector on the right. Secondary electrons are guided by electric fields to start and stop MCPs. Structure in black is held at 1-2 kV positive relative to structure in grey. The detector on the right may be an MCP or a solid-state detector to measure energy (see Section 3). Left: Electrons cross before reaching the start and stop MCP. Grids after the foil and in front of the detector at positive potential are often used to accelerate the electrons more quickly to reduce dispersion. Right: Electrons are reflected by a dual electrostatic mirror, which also facilitates 2-D position sensing.

The main objective of the TOF section is to determine the speed v of the particles and thus their energy E per mass unit A in front of the entrance foil according to:

$$\frac{E_{TOF}}{A} = \frac{1}{1-\alpha_1}\frac{Da}{2}\left(\frac{d}{\tau}\right)^2 \qquad [3]$$

Da (1 Dalton) is the atomic mass unit (1/12 of the carbon atom mass), α_1 is a parameter that reflects the energy loss in the entrance foil. For each TOF sensor this energy loss is determined by a combination of simulation [e.g. Ziegler et al., 2015] and calibration. The TOF resolution $\Delta\tau/\tau$ depends mainly on three characteristics:

1) The energy loss in the foil is a statistical process and thus associated with energy straggling that increases with foil thickness, decreasing particle energy, and increasing mass. Large efforts have gone into reducing the foil thickness [e.g. McComas et al., 2004] and/or into boosting the energy of incoming ions with a high post-acceleration voltage, as described in Section 4.1 and 4.2.

2) The secondary electrons arrive at each MCP with a time dispersion, which can be minimized by their immediate acceleration with a grid on the positive acceleration potential right in front of the foil and the detector at the end, as shown in the electrostatic mirror configuration in the right panel of Figure 2. Such grids have also been used in the overcrossing configuration on the left, for example in AMPTE SULEICA [Möbius et al., 1985a].

3) Due to a finite FoV angle range and additional angular scattering in the foil that is causally connected with the energy straggling, the actual flight d' path may be longer than d according to $d' = d/\cos\theta$, where θ is the angle of the flight path relative to the normal direction of the foil plane. The angular range may be reduced by a long and slender TOF system geometry. Alternatively, in the electrostatic mirror configuration, the start and stop position can be measured with MCP position sensing, providing the information to correct the flight path d'.

Typically, energy straggling (1) dominates the overall TOF resolution $\Delta\tau/\tau$ at low energies because it becomes rather strong. For high-energy or high-speed particles, the electron time dispersion (2) along with the timing accuracy of the electronics dominate, because this is a fixed amount for a given instrument concept, while the TOF τ decreases with speed. A finite angular range (3) leads to a fixed ratio $\Delta\tau/\tau$ and thus a constant contribution to the overall resolution.

As is evident, to measure the TOF τ both the start and the stop signal are needed, thus providing a natural double coincidence, with intrinsic background and noise suppression by orders of magnitude compared with single signal detection techniques. Assuming a noise or background detection rate R_N with a single MCP the statistical background contribution R_{BG} to the TOF rate that competes with a TOF signal with timing resolution $\Delta\tau$ can be estimated as:

$$R_{BG} = R_N^2 \cdot \Delta\tau \tag{4}$$

For a TOF resolution of a few nsec even noise rates of a few kHz are reduced to rates well below 0.1 sec^{-1}. However, the presence of a majority species, typically H, can provide challenges to the detection of minor species with abundances many orders of magnitude below that of H. The detection efficiency for secondary electrons is always lower than 100%. Therefore, particles whose start signal was not detected but their stop signal was may produce chance coincidence events with other ions that had a start signal. Assuming an incoming rate R_{IN} of the majority species, the resulting chance coincidence background rate R_{BG} is:

$$R_{BG} = (1-\mu_{Start}) \cdot \mu_{Stop} \cdot R_{IN}^2 \cdot \Delta\tau \tag{4a}$$

where μ_{Start} and μ_{Stop} are the start and stop efficiencies for the majority species. While Equation (4a) still contains the coincidence related background suppression term $R_{IN}\,\Delta\tau$, the background rate now increases with the square of the incoming rate.

In general, a TOF sensor provides a speed or energy per mass measurement, while simultaneously giving noise and background suppression. This detection technique works equally well for incoming ions or neutral atoms. In order to determine the mass number A and/or the ionic

charge state Q (where a neutral atom has $Q = 0$) of the combination of a TOF system with other measurements that determine the total energy E and/or the energy per ionic charge E/Q is necessary. From the combination of different energy analysis techniques with a TOF subsystem a family of TOF sensors emerges, each of whose members can be optimized for a suitable range of specific applications tailored to the goals of a space mission. A number of technological challenges with TOF spectrographs are addressed by McFadden [2016].

3. Suprathermal/Energetic TOF Spectrographs

As pointed out in the introduction, the suprathermal energy range had been challenging to cover with species-sensitive particle sensors before the advent of the TOF method. Indeed the first TOF spectrographs were implemented for this energy range on satellites in the 1980's. The first mission to contain several TOF spectrographs was the Active Magnetospheric Particle Tracer Explorers (AMPTE) mission [Bryant et al., 1985], with three such instruments, the Medium Energy Particle Analyzer (MEPA) [McEntire et al., 1985] and the CHarge Energy Mass (CHEM) [Gloeckler et al., 1985] sensor on the Charge Composition Explorer (CCE) and the SUprathermal Low Energy Ion Charge Analyzer (SULEICA) [Möbius et al., 1985a] on the Ion Release Module [IRM].

The MEPA sensor is an example for the combination of a TOF system with solid-state detectors (SSD) to determine separately the residual energy E_{Res}, i.e. the energy of E of the incoming article reduced by the fraction α_1 lost in the entrance foil and the fraction α_2 in the contact layer of the SSD. This detector, where the particles are stopped and deposit their energy, is included in the schematics in Fig. 2. Having determined the energy per mass E/A in Equation (3) we now obtain the atomic mass A of the particle according to:

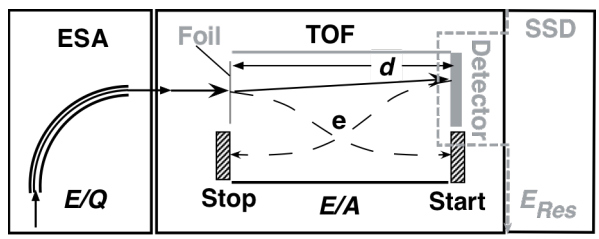

Fig. 3: Schematic view of an ESA-TOF combination with an SSD. The ESA serves as E/Q filter. The TOF spectrograph provides the energy per mass E/A according to Equation 3. The SSD measures the residual energy E_{Res}, and thus allows a separate determination of E, A, and Q.

$$A = \frac{E_{\mathrm{Res}}}{(1-\alpha_2)\cdot E_{TOF} / A} \tag{5}$$

As α_1 the energy loss α_2 is energy and species dependent and is determined by calibration with known ion beams at an accelerator. It is evident that the total energy E can also be determined.

The MEPA sensor was implemented with the electrostatic mirror. To cope with the high intensity of penetrating radiation in the radiation belts and ring current, MEPA included a second foil at the center grid of the electrostatic mirror. From here the secondary electrons were accelerated to a third MCP in the corner of the sensor to provide another independent coincidence measurement, which substantially reduced the background. Other examples of this sensor type are SAMPEX LICA [Mason et al., 1990; Mason et al., 1993], ACE ULEIS [Mason et al., 1998], and STEREO SIT [Mason et al., 2008]. To boost TOF resolution and reduce background, ULEIS contains two consecutive electrostatic mirror TOF sections. This sensor allowed abundance measurements of ^{3}He in small impulsive energetic particle events even below 1%, thus establishing that selective acceleration of ^{3}He is indeed a hallmark of all impulsive events. Enhanced ^{3}He

abundances were even found in coronal mass ejections indicating re-acceleration of remnant impulsive populations [Mason et al., 2005; Desai et al., 2006].

To separately determine E, A, and the ionic charge state Q of incoming ions the combination with an electrostatic analyzer (ESA) at the sensor entrance is needed. The AMPTE CHEM and SULEICA instruments were the first satellite borne TOF spectrographs to provide that capability. A schematic view of the SULEICA sensor is shown in Fig. 3. The ESA acts as energy per charge filter, which passes ions within a narrow band with a specific E/Q and resolution $\Delta E/Q$. The mass per charge ratio is determined as:

$$\frac{A}{Q} = \frac{E/Q}{E_{TOF}/A} \tag{6}$$

making use of $E/Q = E_{TOF}/Q$, where E_{TOF} is obtained from Equation (3). As a consequence, the full energy range is covered by changing the ESA voltage in logarithmic steps. The number of energy steps n determines the duty cycle of the sensor, and its effective geometric factor is reduced by the factor n. We will turn to potential improvements in Section 4.2.

Typically, the ions are first separated according to A/Q with the combined resolution of the ESA and the TOF section according to:

$$\frac{\Delta A/Q}{A/Q} = \sqrt{\left(\frac{\Delta E/Q}{E/Q}\right)^2 + 2\left(\frac{\Delta\tau}{\tau}\right)^2} \tag{6a}$$

The ESA resolution is constant for a given analyzer, whereas the TOF resolution varies with species and energy. The resolution in mass A is a combination of the TOF resolution and the energy resolution of the SSD.

$$\frac{\Delta A}{A} = \sqrt{\left(\frac{\Delta E_{\mathrm{Res}}}{E_{\mathrm{Res}}}\right)^2 + 2\left(\frac{\Delta\tau}{\tau}\right)^2} \tag{6b}$$

Equations (6a) and (6b) are good approximations as long as the contributing resolution ratios are small compared to one. Both the TOF and the energy resolution increase rapidly for low particle energies. Because the energy range of CHEM extends into the bulk plasmas of the magnetosphere and the solar wind, this sensor includes post-acceleration to boost the ion energy for the TOF and energy measurement [Gloeckler et al., 1985], as discussed in Section 4.3.

The A/Q resolution of SULEICA alone was key for the discovery of interstellar He^+ pickup ions [Möbius et al., 1985b] in conjunction with detecting Li^+ [Möbius et al., 1986] from the cloud experiments in the solar wind conducted with the AMPTE IRM satellite [Haerendel et al., 1985]. The combination of A/Q resolution and total energy measurement allowed the unambiguous identification of energetic NO^+ and O_2^+ ions in a post-storm ring current [Klecker et al., 1986], because molecular ions typically break up when passing the TOF entrance foil. In this way, suprathermal TOF mass spectrographs opened the door for many studies, which were not possible before. Other examples of this sensor type are WIND STICS [Gloeckler et al., 1995] and SOHO STOF [Hovestadt et al., 1995].

4. Low Energy TOF Spectrographs for Bulk Plasmas

Until the 1980's magnetic mass spectrometers dominated the instrumentation in the thermal and bulk plasma regime. However, their limitation to energies below about 15 keV/Q, along with the difficulty to provide a wide angular FoV and their relatively low geometric factor, provided formidable challenges to measure 3-dimensional distribution functions with mass and charge resolution and a reasonably high time resolution.

4.1 Distribution Function Analyzers with A/Q resolution

The realization that only small contributions of a few percent of O^+ ions to magnetospheric plasmas or 10% of He^{2+} ions to the solar wind would have a substantial contribution to the momentum balance in physical processes, such as reconnection and bulk acceleration led to an alternate approach that includes the TOF method. Thus, for Cluster and simultaneously for FAST and Equator-S a sensor concept was developed based on a marriage between a top-hat ESA, as used successfully in the 3D Plasma instrument [Paschmann et al., 1985], and the TOF section of the SULEICA sensor [Möbius et al., 1985a], both on AMPTE IRM. For the new sensor, the TOF section was expanded to a fully rotationally symmetric cylindrical geometry [Möbius et al., 1998a; Réme et al., 1997; Klumpar et al., 2001]. Because the most important ion species in the magnetosphere (H^+, He^{2+}, He^+, O^{2+}, and O^+) are separated in A/Q by subsequent factors of two an implementation could be chosen that consists solely of an ESA and a TOF section to determine E/Q and E/A, albeit with post acceleration of the ions between ESA and TOF section with a negative voltage up to -20 kV.

Figure 4 includes a cross-sectional and a top view of the COmposition and DIstribution Function (CODIF) sensor. The top-hat ESA, for which the lower part of Fig. 4 represents a radial cut of the fully rotationally symmetric configuration, allows instantaneous coverage up to 360° in elevation angle θ and typically $\Delta\phi$ = 6-15° in azimuth. Each spin is sub-divided into 32 spin angle (ϕ) sectors during each of which the ESA voltage is swept through its full range to provide energy coverage. For Cluster CODIF and Equator-S ESIC, each sweep is sub-divided into 128 logarithmically spaced steps, while FAST TEAMS uses 192 steps. The Cluster CODIF and the Equator-S ESIC sensors have a split FoV with two 180° wide apertures and geometric factors that differ by about x50 to increase the dynamic range and to allow accommodation of a retarding potential analyzer for the lowest energies [Réme et al., 1997]. FAST TEAMS makes use of the full 360° aperture with identical geometric factor and thus obtains a full distribution function within ½ spin. The relevant E/Q for the TOF section includes the

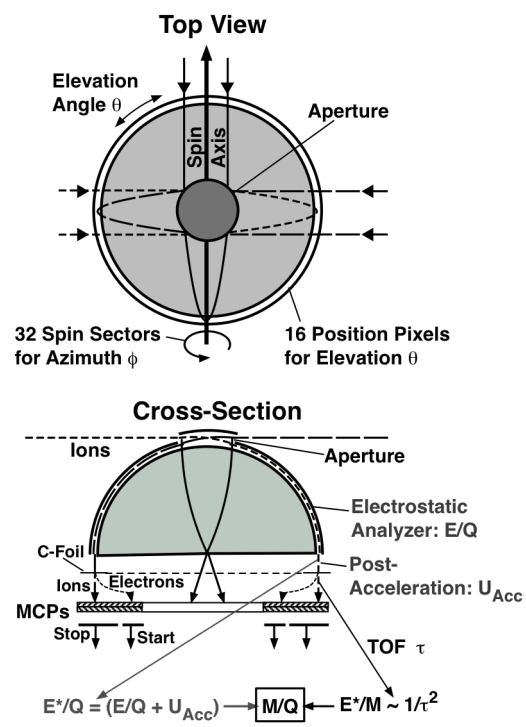

Fig. 4: Top view and cross-sectional view of the CODIF sensor. The top-hat ESA provides imaging of elevation angle θ to a position at the exit, which the start electrons map to 16 sectors of the start MCP. Spin covers azimuth ϕ because the sensor symmetry axis is oriented at 90° relative to the spin axis.

post-acceleration voltage U_{PAC}, thus modifying Equation (6) to:

$$\frac{A}{Q} = \frac{E/Q + U_{PAC}}{E_{TOF}/A} \qquad (7)$$

The design challenges and choices for this sensor were described by Möbius et al., [1997] in connection with the previous space instrumentation symposium and in the instrument papers, and thus shall not be repeated here. The sensors on Cluster, FAST, and Equator-S have led to numerous studies that would have been impossible without the fast coverage of the distribution function and the species identification, for example: differential acceleration of ions in the auroral region [Lund et al., 1998; Möbius et al., 1998b], acceleration of He^+ by electromagnetic ion cyclotron waves in the inner magnetosphere [Mouikis et al., 2002], the importance of the cusp as a source for O^+ in the magnetotail [Kistler et al., 2010], and the role that O^+ plays in magnetic reconnection in the magnetotail [Liu et al, 2015] and at the magnetopause [Wang et al., 2015].

4.2 TOF Sensors with Post-Acceleration that Provide Charge State

While the most abundant ion species in the Earth's magnetosphere as well as interstellar pickup ions can be distinguished unambiguously with an ESA – TOF combination, a meaningful composition analysis of the solar wind and related suprathermal particles requires a three-dimensional analysis [E/Q, E/A, E], including residual energy measurement with an SSD. To distinguish between neighboring charge states of, for example, C and O, a combined resolution in A and Q of better than ΔA, $\Delta Q \leq 1$ is needed. To achieve such resolution post-acceleration voltages in excess of 20 kV [Gloeckler et al., 1992], ultra-thin C-foils [Funsten, et al., 1994], and SSDs with very good energy resolution and thin dead layers are needed. A typical instrument for solar wind composition measurements is Ulysses and ACE SWICS [Gloeckler et al., 1992; 1998]. The sensor is similar to the one in Fig. 3, but with post-acceleration between the ESA and the TOF section. Now the entire TOF section, including SSD and analog electronics is at the post-acceleration potential. Like AMPTE SULEICA and Cluster CODIF, SWICS takes advantage of the spinning Ulysses and ACE spacecraft to obtain angular distributions. With the spin axis pointing close to the Sun, the SWICS FoV of 70° in the direction perpendicular to the spin plane guarantees almost continuous coverage of the solar wind and extensive coverage of pickup ions.

The other two solar wind composition TOF spectrographs, SOHO CELIAS CTOF [Hovestadt et al., 1995] and STEREO PLASTIC [Galvin et al., 2008], were implemented on three-axis stabilized spacecraft that were optimized for Sun viewing optical and EUV cameras. With the large collecting power of its 180° hemispherical electrostatic analyzer situated between two quadrupole lenses and un-interrupted coverage of the solar wind, CTOF provided the first high time resolution measurements of solar wind composition. Like its predecessor CTOF, STEREO PLASTIC provides un-interrupted and high time resolution for solar wind ion measurements, but PLASTIC also provides the first full directional information for solar wind heavy ions. The entrance system for PLASTIC [Blush et al., 2005] is a 360° top-hat electrostatic analyzer that incorporates three different geometrical factors. In the sunward direction, two sets of electrostatic deflectors are also used in order to provide 40° coverage in the out-of-ecliptic direction. For solar wind ions, the largest geometric factor is reduced automatically by electrostatically switching to the smallest aperture during each ESA stepping cycle, when high He^{2+} and H^+ fluxes are encountered [Galvin et al., 2008]. In this manner, reliable measurements over the entire dynamic range of suprathermal and solar wind ion populations can be obtained in each 1-

minute cycle. In contrast, on other missions, an additional sensor is included in the payload for the purpose of measuring solar wind protons and alphas. Like SWICS and CTOF, the PLASTIC TOF section incorporates SSDs to allow full mass and charge measurements.

Among others, Ulysses and ACE SWICS have allowed great advances toward the composition, velocity distribution, and spatial distribution of pickup ions [Gloeckler & Geiss 1998; Gloeckler et al., 2004; Chen et al., 2013]. They have demonstrated distinct mass and charge composition differences between fast and slow solar wind and their variations with solar activity [vonSteiger et al., 2000] as well as great insight into coronal mass ejection related solar wind [Lepri et al., 2001] and their likely source populations. The unique high angular resolution of STEREO PLASTIC has recently allowed the unambiguous demonstration that interstellar He^+ pickup ions maintain a narrow toroidal velocity distribution from the original injection for quite a while during their transport with the solar wind [Drews et al., 2015]. The temporal resolution of SOHO CTOF and STEREO PLASTIC (e.g., 5-10 minute for an iron spectrum) has enabled distinguishing differences in the magnetic field and ion compositional boundaries of solar wind structures [e.g., Aellig et al., 1998; Galvin et al., 2013; Winslow et al., 2016].

4.3 Efforts to Improve Resolution, Temporal Cadence, and Reduce Sensor Size

One key capability of the various plasma TOF spectrographs is their ability to separate individual species and charge states. However, to resolve unambiguously the charge states of neighboring elements, the minimum energy before entry of the TOF section has to be boosted by post-acceleration to relatively high voltages and/or the energy resolution of SSDs has to be improved, in particular for low energy ions. However, providing isotope resolution requires a different TOF section concept that sacrifices ionic charge resolution and will be discussed in Section 5. An extremely challenging method to improve the overall resolution, albeit with some recent success in the laboratory, is to push the post-acceleration voltage to 50 - 100 kV, as presented by Gilbert et al. [2016], which would lead to energy, mass, and charge resolution comparable to a suprathermal or energetic particle sensor. Alternatively, the use of an ultra-thin window and low noise SSDs in the form of Avalanche Photodiodes (APD) or novel diamond detectors [Ogasawara et al., 2015], is being explored, which may also allow the combination of energy measurement and stop detection in the same detector and thus could reduce sensor complexity.

The increased complexity of instruments like PLASTIC to provide angular coverage and resolution as well as simultaneous optimization for full mass and charge resolution of the solar wind proper, along with the dual need to increase time resolution for reconnection studies and to reduce the size and complexity of sensors for smaller spacecraft missions, have prompted the search for alternative sensor concepts. One key obstacle to improving time resolution and reducing sensor size, while maintaining a high effective geometric factor, is the intrinsic requirement to step through the ESA voltage. Including the scan in at least one angle, either via the spacecraft spin or with a deflector system, this amounts to nested scans in two dimensions of velocity space. This greatly impacts both time resolution and effective geometric factor because of the low measurement duty cycle. Therefore, several attempts have been and are being made to eliminate one of the scans, either in energy or angle by a scheme that allows simultaneous coverage.

The MESSENGER FIPS sensor is a successful attempt to reduce the sensor size and eliminate the need of angular scanning by combining a wide-open ESA with a collimator and position sensing at the interface between ESA and TOF section to obtain the arrival angle for a selected E/Q range [Andrews et al., 2007; Zurbuchen et al., 2016]. A somewhat different and

conceptually simplified way to obtain a simultaneous image of the velocity distribution with a FoV of almost 2π has been presented by Skoug et al. [2016]. Here, the ESA is the region between a planar entrance plate with a center pinhole aperture and a filterplate at the exit, which only passes ions of a pre-determined ratio $E/(Q\,U_{ESA})$. Yet ions that arrive from a range of elevation angles θ are identified simultaneously, where θ translates into a unique radial position $r(\theta)$. A challenge of this design is obtaining a reasonable energy resolution for particles that arrive at elevation angles close the center axis of the sensor because the deflection field is almost in the direction of motion. To improve this resolution an additional center cone at the potential of the collimator plate is introduced, which provides a radial deflection field component.

Another attempt to improve the temporal cadence by providing partial imaging of a combination of elevation angles and energy per charge has been made with an ESA curvature that depends on the azimuth angle of the instrument aperture. The Advanced Mass and Ionic Charge Composition Experiment (AMICCE) provides simultaneous coverage over a range of energies, thus reducing the number of energy steps by about a factor of ten [Allegrini et al., 2009; 2016]. With a "flower-shaped" ESA that has a wide opening at the entrance and exit, but is narrow in its middle, the SupraThermal Ion Monitor (STIM) provides simultaneous coverage over a range in energy and imaging of about 40° in elevation angle [Desai et al., 2015; Desai et al., 2016]. Elevation angle and E/Q are obtained by position sensing at the detector.

5. High-Resolution TOF Spectrographs

Linear TOF spectrographs are limited in their resolution by the spread in energy E and angle θ due to scattering in the C-foil according to $\Delta\tau/\tau \sim \sqrt{\Delta E/E}$ and $\Delta\tau/\tau \sim \sqrt{1-cos2\Delta\theta}$. Uncertainties in the TOF electronics can be held at typically <0.5 ns and are mostly negligible. As discussed already in Section 2, the energy and angle scattering are inherent in the design of linear TOF spectrographs and, as discussed in Section 4, can only be mitigated within limits by the choice of very thin C-foils and/or high post-acceleration voltages. Because the TOF resolution is directly linked to the M/Q and M resolution of the instrument (Equation 3a and 3b) separation of neighboring elements and isotopes call for a different instrument concept. Alternate TOF spectrometry concepts that avoid a foil as start sensing element are in use for specific applications. A rotating electric field, which ties the start timing to the phase of the field, provides a successful alternative to magnetic gas analyzers, but without access to the velocity distribution function. An example is the STROFIO sensor on Bepi Colombo [Orsini et al., 2010; Livi 2016]. Gated TOF spectrographs that derive the timing by short opening pulses of the system are useful to diagnose high bulk ion fluxes when a small duty cycle of the sensor due to the short opening pulse compared with the TOF window can be afforded [Orsini et al., 2010; Paschalidis 2016]. Here, we concentrate on isochronous TOF geometries.

5.1 Isochronous TOF Spectrographs

To eliminate the uncertainties related to the energy and angle straggling, a TOF configuration has been implemented, in which the ions follow a ballistic trajectory in a retarding electric field whose strength increases linearly with distance from the common plane of the entrance foil and stop detector as shown in Fig. 5 [e.g. Managadze 1986]. The linearly increasing electric field $E(y) = k \cdot y$ turns the TOF sensor into a harmonic oscillator and τ becomes half the oscillator period, which solely depends on the ion mass per charge A/Q. The majority of ions in the energy

range 1 to 30 keV/e leaves the entrance foil of the TOF system as neutral atoms or as singly charged ions [Gonin et al., 1992]. For the ions, the τ obeys:

$$\tau = \frac{\pi}{\omega} = \pi\sqrt{\frac{A \cdot Da}{ek}} \tag{8}$$

which requires a retarding potential of ≈20 kV for 45° trajectories. Neither initial energy nor incoming angles affect the resulting TOF τ in the reflecting section, which solely depends A for singly charged ions, thus making the mass resolution also independent of the ESA *E/Q* resolution. For an earlier review see Wüest [1998]. Neutral atoms that leave the TOF section on a straight line can be analyzed in an additional linear TOF section (in purple in Fig. 5). To obtain also the energy of the ions an electrostatic *E/Q* filter is placed in front of the TOF entrance.

The reflecting electric field, which increases linearly with distance from the plane that contains entrance foil and stop MCP, is key to the harmonic oscillator behavior. Such a field configuration can be implemented with a series of potential shaping electrodes, as in CASSINI CAPS [McComas, et al., 1998], or the bounding electrodes are shaped such that they represent the appropriate boundary conditions for the solution of Laplace's equation for a potential that increases with the square of the distance from the entrance plane. This condition has been achieved with a set of V-shaped electrodes for a mostly planar geometry of the ion trajectories in the TOF section, as depicted in Fig. 5, for WIND MASS [Gloeckler et al., 1995] and SOHO CELIAS MTOF [Hovestadt et al., 1995]. The ROSINA experiment on ROSETTA to study elementary, isotopic, and molecular composition of comet 67P/Churyumov–Gerasimenko contains the isochronous TOF sensor RTOF, but also includes a magnetic spectrometer for the mass resolution required to separate neighboring heavy molecular species [Balsiger et al., 2007]. To potentially combine a reflecting TOF section with a top hat ESA that can obtain instantaneously a 360° slice of the ion velocity distribution, a cylindrically symmetric potential configuration is used in the CYLMAS concept [Möbius et al., 1990; Gubler et al., 1995].

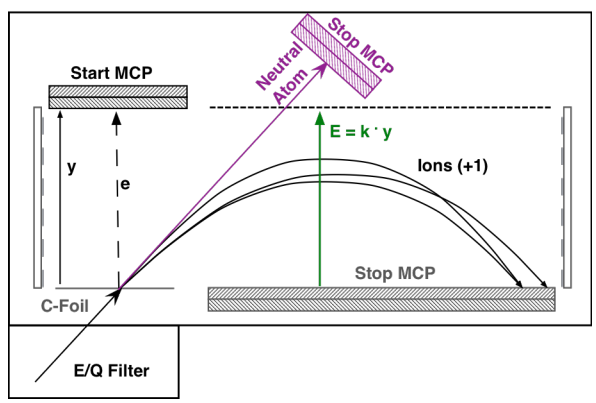

Fig. 5: Schematic view of a reflecting TOF spectrograph. In the linearly increasing electric field ions that leave the start foil perform half a harmonic oscillation, whose TOF τ only depends on M/Q, before reaching the stop MCP. Particles that leave the foil as neutral atoms can be analyzed in a linear TOF section (in purple). To obtain the original energy, an E/Q filter may be added to the sensor entrance.

5.2 Solar Wind Isotope Observation

WIND MASS [Gloeckler et al., 1995] and SOHO CELIAS MTOF [Hovestadt et al., 1995] have indeed provided great insight into the solar wind isotope composition and have expanded on the initial measurements taken with solar wind collector foils during the Apollo missions on the moon's surface [Geiss et al., 1972]. The isotope composition of the solar wind is the best proxy that we can currently obtain on the Sun's isotope composition, which in turn is an archive of the element forming processes in the galaxy [Geiss & Reeves 1972] and of the fractionation processes during the solar system formation [Marti & Bochsler 2012]. The solar corona and thus the solar wind do not necessarily share an unbiased isotope composition with the Sun's

interior [Bochsler 2000]. Thus any variations of the isotope ratios with solar wind type and speed will help to unravel fractionation processes between the Sun and the solar wind. To this end, measurements with isochronous TOF sensors have enabled the differentiation between solar wind types, whereas the foil collector technique largely provided average values. A compilation of solar wind composition, with substantial emphasis on isotopes, may be found in the paper by Wimmer-Schweingruber [2002]. The Isochronous TOF mass spectrographs have expanded the number of elements now accessible to solar wind isotope observations, including elements up to the mass of iron.

Wimmer-Schweingruber [2002] compared solar wind isotope ratios, among them for Ne and Ar, as obtained with SOHO MTOF [Kallenbach. et al., 1997] and with the Apollo foil collectors [Geiss et al., 1972]. All values agree within their observational uncertainties, which serves as a validation of both techniques. Furthermore, the Mg isotope ratios [Bochsler et al., 1997; Wimmer-Schweingruber et al., 1999] show a significant difference between fast and slow solar wind. The values for coronal mass ejections appear to agree within their uncertainties with those of the slow solar wind. This isotope fraction appears to be connected to a dependence of the Mg isotope ratios on solar wind speed [Kucharek et al., 1998], also confirmed by Kallenbach et al., [1998]. A likely reason for this fractionation may be found in the inefficient Coulomb drag in the corona [Bodmer & Bochsler 1998].

5.3 Improvement of TOF Mass Resolution without Reflection

While the reflecting TOF scheme appears to be an ideal solution for an isotope-resolving TOF mass spectrograph, it comes with challenges and shortcomings. Firstly, the reflecting electric field requires an additional high voltage supply for rather high voltages to cover a reasonable energy range. Secondly, the retarding field naturally defocuses the ion trajectories. As a consequence, the already existing angular dispersion after the entrance foil increases substantially so that only a small fraction of the incoming ions are detected at the stop detector, thus reducing the effective geometric factor of this spectrograph typically by more than one order of magnitude over that of a linear TOF system. Therefore, alternatives to improve TOF resolution needed.

What limits the TOF resolution of a linear TOF spectrograph most severely is the energy and angle straggling during the ion passage through the foil. Therefore, much effort has gone into reducing the foil thickness [Funsten et al., 1994; McComas et al., 2004]. A potential alternative is the suggestion to replace the foil as the secondary electron generating element with a single-stage MCP [Devoto et al., 2008]. Instead of penetrating the material of a thin foil, the ions bounce off the surface inside the electron multiplication channels of the MCP at glancing angles. In this way, the energy loss and thus the energy straggling is very small, and the range of angles into which the ions are scattered is very narrow around the angle of specular reflection. The very long and narrow MCP channels restrict the angle range further. In addition, the number of secondary electrons leaving the MCP

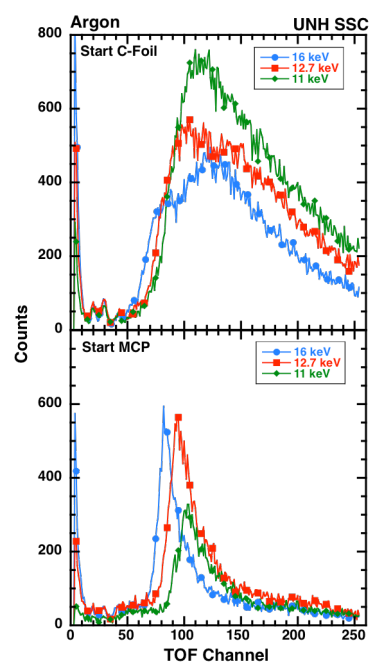

Fig. 6: TOF spectra of 11, 12.7 and 16 keV Ar using a ≈3.5 μg/cm^2 C-foil (top) and a single stage MCP (bottom) as start window.

may already be amplified by a factor that depends on the voltage applied across the MCP.

For a side-by-side comparison of the C-foil and MCP performance in an identical sensor configuration, the C-foil has been replaced by a single-stage MCP in one of the 16 sectors of the TOF section. A 3.5 μg/cm^2 C-foil was compared with an MCP, whose channels have a 25 μm diameter and a length to diameter ratio $l/d = 20$. Figure 6 shows TOF spectra taken with an Ar^+ beam at energies of 11, 12.7 and 16 keV. The C-foil spectra are shown on the left and the ones with the MCP on the right. A remarkable reduction in the width of the TOF spectra with the MCP entrance is evident. For 11 keV, the full width at half maximum is reduced by almost a factor of 3 from ≈125 to ≈45 TOF channels. Because of its high mass, Ar is usually an extremely challenging species to obtain a TOF spectrum at such low energies. Building on advanced atomic layer deposition, this test setup is also being used to test the reflectivity, scattering characteristics, and secondary electron yield of several different MCP channel coatings.

The finite open area ratio of the MCPs and their limited opening solid angle reduces the transparency of the sensor entrance window and consequently the start efficiency of the TOF section. Results presented by Cadu et al. [2016] show that such efficiency reductions are partially compensated by the MCP gain and that they are definitely much smaller than the effective geometric factor reduction of isochronous TOF systems compared with linear TOF systems.

6. Energetic Neutral Atom Spectrographs

TOF mass spectrographs work just as well for neutral atoms as they do for ions. Whether a neutral atom or an ion passes through the thin entrance foil does not affect the number of secondary electrons emitted, and the average charge state upon exit from the foil only depends on the energy and species of the particle [Gonin et al., 1992]. Therefore, TOF spectrographs can also be used to analyze energetic neutral atoms [ENAs]. Neutral atom populations are ubiquitous in the solar system, in planetary, lunar, and cometary atmospheres, as well as in the interstellar gas flow through the heliosphere.

The simultaneous presence of plasmas and neutral gas provides for a very effective remote sensing technique of ion velocity distributions in the heliosphere for populations that are found at a large distance from the observer. Because charge exchange occurs through the transfer of an electron from the neutral gas atom, with the electron mass negligible compared to that of the parent ion, the daughter ENA maintains the original ion momentum. Therefore, the ENA velocity distribution mimics that of the parent ion distribution, modified by any speed dependence in the charge exchange cross-section $\sigma_{\mathrm{ChEx}}(v)$. ENAs are not deflected by electric or magnetic fields on their way to the observer and arrive on straight trajectories, only modified by gravitational deflection [e.g. Kucharek et al 2015], radiation pressure, ionization losses [Bzowski et al., 2013], and collisions. Before corrections for the aforementioned effects, the observed differential ENA fluxes J_{ENA} as function of energy E and solid angles θ and ϕ are related to the parent ion velocity distribution $f_i(v, \theta, \phi)$ according to:

$$\frac{dJ_{ENA}(E,\theta,\phi)}{dEd\Omega} = n_a \sigma_{ChEx}(v)\Delta l \cdot \frac{v^2}{m_i} f_i(v,\theta,\phi) \tag{9}$$

n_a is the density of the surrounding neutral gas, Δl is the length along the line-of-sight over which the charge exchange interaction occurs, and m_i is the mass of the ion. The factor v^2/m_i provides the transformation from velocity distribution to differential flux as in Equation (1). One of the biggest challenges to making reliable observations of ENAs is the competition from typically

much higher fluxes of ions at comparable energies. These ions must be suppressed before entering the sensor, or they must be carefully distinguished inside the sensor system, because the detectors are equally sensitive to ions and neutral atoms. Of course, other background sources for particle measurements, such as photons, electrons, and penetrating cosmic rays have to be eliminated or at least well characterized.

6.1 Suprathermal Neutral Atom Spectrometers

Because ions and neutral atoms produce secondary electrons at the TOF entrance foil with comparable efficiencies suprathermal and energetic particle TOF spectrographs without an ESA entrance system, such as SAMPEX LICA or ACE ULEIS [Mason et al., 1998], can also work as ENA mass spectrographs. However, they need an electrostatic suppression scheme at the entrance aperture so that ENAs can be identified unambiguously. The first sensor equipped in this way is the SOHO CELIAS HSTOF section of the STOF sensor [Hovestadt et al., 1995]. A schematic view of this sensor is shown in Fig. 7. The entrance collimator consists of a set of plates that deflect ions of energies up to the upper limit of the ENA energy range E_U/Q to hit the plates, and thus they do not enter the sensor system. Ions with energies higher than E_U/Q will enter, and thus this sensor will serve a dual purpose, as ENA sensor for $E_{ENA} < E_U$, and as ion sensor for $E_{Ion}/Q > E_U/Q$. HSTOF is the high-energy ion section of the CELIAS STOF sensor, with a substantial overlap with STOF over the energy range 150 – 600 keV/Q. This overlap allows an additional validation and separation of ion fluxes that might interfere with the ENA spectrum.

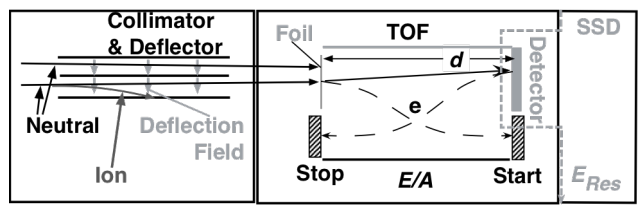

Fig. 7: Schematic view of a suprathermal ENA mass spectrograph. A mechanical collimator (left) with electrostatic deflection filters out incoming ions in the energy range of the ENA observation. The TOF section (right) is similar as in section 3.

These unique capabilities have enabled the HSTOF sensor to obtain heliospheric ENA distributions in the energy range 55-150 keV [Hilchenbach et al., 1998]. They used the fact that the energy spectra of H ENAs and H^+ seen by HSTOF and STOF above 150 keV match to conclude that there is indeed a substantial excess of H ENAs below 150 keV, increasing toward lower energies. This comparison validated that HSTOF indeed sees H ENAs, unambiguously distinguished from interfering backgrounds. The maximum of this ENA flux appears to come from the heliotail direction [Hilchenbach et al., 1998]. In addition, He ENAs have been identified with HSTOF [Czechowski et al., 2004].

While SOHO HSTOF was primarily designed as an energetic ion TOF mass spectrograph and the ENA separation capability was included only during the implementation phase, other ENA detectors were optimized specifically for that purpose. As part of the Imager for Magnetopause-to-Aurora Global Exploration (IMAGE) mission the High Energy Neutral Atom (HENA) imager [Mitchell et al., 2000] was optimized specifically for the imaging of magnetospheric ENAs, largely using the same physical principles used in HSTOF. The HENA sensor provided valuable insight into the global dynamics of energetic particles during geomagnetic storms [e.g. Mitchell et al., 2001]. The Cassini probe carries the Ion-Neutral CAmera [INCA; Mitchell et al., 1996] as part the Magnetosphere IMaging Instrument (MIMI) package [Krimigis et al., 2004]. INCA was designed and optimized to image Saturn's magnetosphere and its interaction with the moons, but it also provides images of the heliospheric boundary region [Krimigis et al., 2009]

through ENAs at energies above the range covered by the Interstellar Boundary Explorer (IBEX) mission [McComas et al., 2009a].

6.2 Low Energy Neutral Atom Spectrographs

In a similar way, low energy ion TOF mass spectrographs can be used for low energy neutral atoms as well. The main challenge is that neutral atoms cannot be manipulated with electric and magnetic fields like ions. In particular, an ESA is needed to determine the energy of low energy particles, and, as discussed in Section 4, ions at energies below about 10 keV/Q need to be post-accelerated to obtain a reasonable TOF and thus mass resolution. Therefore, in all low energy sensors ENAs are converted into ions after they have passed a collimator at the entrance, which allows the determination of their arrival direction.

All low energy ENA sensors contain the same building blocks as shown in Fig. 8. The sensor aperture and electrostatic deflection and/or repeller scheme rejects electrons and ions from entering the collimator. A mechanical collimator selects the arrival direction and determines the sensor FoV for the incoming ENAs. Then the ENAs are converted to ions. For medium low energies, typically 0.5 – 10 keV, an ultra-thin C-foil is used to strip off electrons to convert atoms to positive ions. The fraction of neutrals that become ions depends on species and energy [Gonin et al., 1992]. Such a sensor has been built and optimized for magnetospheric imaging for IMAGE as the Medium Energy Neutral Atom (MENA) imager [Pollock et al., 2000]. For ENA energies between 0.01 and 2 keV, the ENAs undergo a reflection at glancing incidence angles on a highly polished surface and are converted to negative ions, as implemented for IMAGE in the Low Energy Neutral Atom (LENA) imager [Moore et al., 2000] and developed further in Livi et al. [2003]. Fig. 8 shows a configuration of the low energy version of the ENA sensor with reflection off a conversion surface. After conversion, the emerging ions pass an ESA for energy selection and then are post-accelerated. The final functional block is a TOF mass spectrograph, or, if mass analysis is not needed, a coincidence detector system. The implementation of a coincidence system becomes very important for ENA cameras because the expected ENA fluxes are generally extremely low compared with those of ions in the same energy range and also compared to any background generating signals. Therefore, the coincidence of two or more related signals that are generated by the incoming ENAs are required to distinguish the weak signal from any kind of background. Low energy ENA imagers that employ surface conversion to positive ions and the subsequent bounce on a surface with secondary electron generation as start signal are used for planetary applications [e.g. Barabash et al. 2006, 2009]. Here, we concentrate on heliospheric applications with their background related challenges.

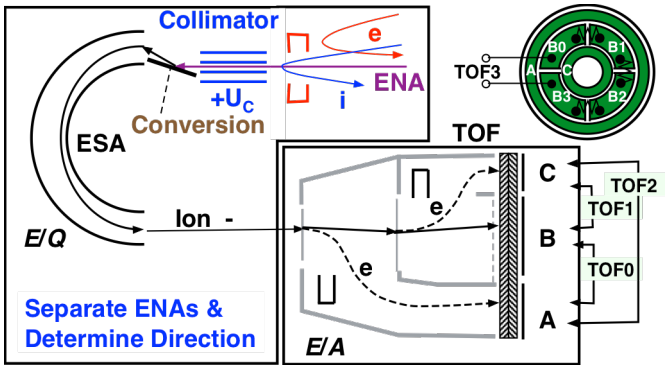

Fig. 8: Schematics radial cut of IBEX-lo. A top view of the signal anodes is shown in the upper right with the 4 quadrant anodes in the Stop portion (B) of the MCP, which are connected by delay lines. All 4 TOF measurements (TOF0, 1, 2, 3) are indicated.

IBEX takes ENA imaging to its current limits by obtaining images of the Heliosphere boundary and sampling directly the neutral interstellar gas flow through the inner heliosphere

[McComas et al., 2009a]. To achieve these goals, particular attention to background and noise suppression was necessary at all steps, as mentioned above [Wurz et al., 2009], because the signal rates that make up the ENA sky maps are extremely low, so that some individual pixels of the maps contain only a few ENA counts per day. Therefore, the IBEX detector units are equipped with genuine triple coincidence systems. IBEX contains two cameras, IBEX-Lo for the low energy range 0.01 – 2 keV [Fuselier et al., 2009] with ENA to negative ion conversion and IBEX-Hi for the medium low energy range 0.3 – 6 keV [Funsten et al., 2009] with stripping of ENAs to positive ions. Funsten et al. [2016] discuss IBEX-Hi and related sensors. Here we will concentrate on the IBEX-Lo TOF spectrograph.

The IBEX-Lo TOF system is adapted from Cluster CODIF [Reme et al., 1997]. Because background suppression is so important for IBEX, two similar TOF sections are nested to provide genuine triple coincidence. Figure 8 shows a schematic radial cut. At the first C-foil, each incoming ion generates secondary electrons that are guided to the outermost section (A) of a single two-stage MCP, while electrons from the second foil reach the innermost section (C). The ions are stopped at the center section, which consists of 4 quadrants (B0-3) for additional background characterization. All sections are electrically separated on the signal anode (upper right in Fig. 8). TOF measurements are made between each of the foils and the MCP (TOF0, TOF1) and between the two foils (TOF2). For additional background characterization, the quadrant position is derived from a delay line along B0-B3 (TOF3).

During the IBEX-Lo background characterization each of the three TOF coincidence rates was lower than 10^{-3} s^{-1}, indicating a very clean and low noise TOF section. Next we turn to the advantages of a triple TOF configuration to reduce chance signal coincidences due to orphaned start and stop signals, as already indicated in Equation 4 and 4a. The additional TOF signal reduces the background rate by another factor $R_{\mathrm{Start}} \cdot \Delta\tau$, where $\Delta\tau$ is the TOF resolution. Figure 9 shows how requiring more TOF signals and successive constraints improve the background response with TOF2 (H1, H2) and TOF0 (H3, H4) histograms and TOF1 vs. TOF0 scatter plots (S1 – S4) from an H atom test with 16 kV post-acceleration. S1, H1, and H3 contain all events with at least one of the three TOF measurements valid. Except for an easily identifiable peak near 0 ns in TOF2 (related to electrons) and two very small "ghosts" (also in S1) near 0 ns in TOF0 the single TOF histograms provide already a clean H distribution [Möbius et al., 2008].

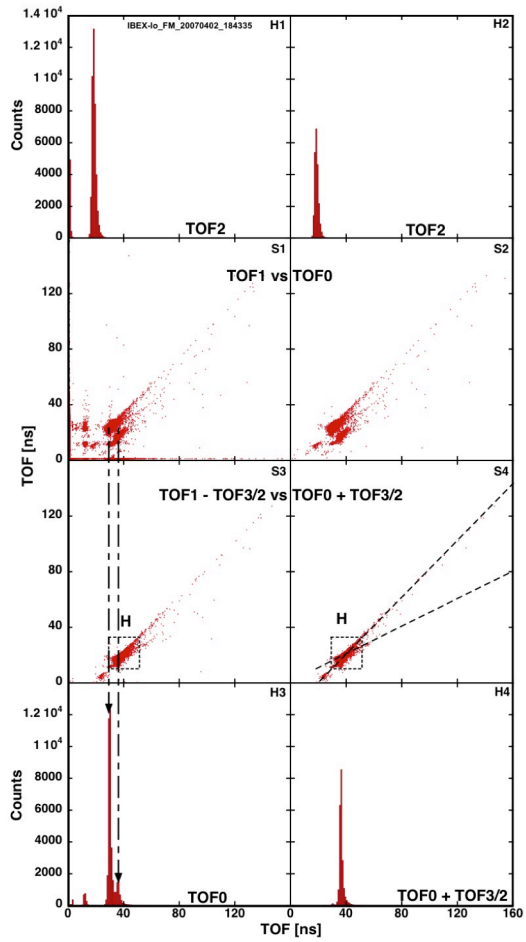

Fig. 9: Sequence of TOF2 histograms H1 and H2, TOF1 versus TOF0 scatter plots that shows the successive removal of background and ghost signals from S1 through S4, and TOF0 histograms H3 and H4, as described in the text [adapted from Möbius et al., 2008; reproduced with the permission of the Institute of Geophysics-UNAM].

S2 and H2 only include events with four valid TOF measurements and which fulfill the checksum condition: |TOF0 + TOF3 – TOF1 – TOF2| < 1ns. Clearly all events with TOF = 0 in one of the channels (no valid TOF) are gone and most of the events outside the H peak region. In H3, S1, and S2 two distinct peaks (connected by arrows) are seen, which come from neighboring MCP quadrants with different delay times. In S3, S4, and H4 this is corrected by using TOF0 + TOF3/2 and TOF1 - TOF3/2 instead, perfectly aligning the H distribution. Only events inside the (dashed) H box remain and a few along two diagonal lines with slopes of 1 and 0.5 (faint dashed lines in S4), due to H energy straggling in the second or first foil, respectively. S3 and S4 show a residual <0.5% peak on the slope 1 line, which stems from cross-talk to the delay line anode and thus also contains legitimate H events. Like the H ENA selection in the flight data, in S4 only events have been selected in TOF2 (H2) that belong to the H peak down to the 1% level, thus requiring consistency between all three TOFs. During a background run over 2.5 days no triple H count was recorded, thus exceeding even our ambitious goal of less than 1 count per day.

In spite of its emphasis on excellent background suppression, the IBEX-Lo TOF subsystem also provides high detection efficiency, which is very homogenous over the entire unit. For highest background suppression triple coincidence is used, and for highest counting statistics any single TOF measurement is accepted. Both efficiencies have been derived from calibrations with neutral beams for the nominal post-acceleration voltage. Even with a post-acceleration voltage that is now reduced to 7 kV from 16 kV after a discharge during a long eclipse, IBEX-Lo works very effectively. It still fulfills all science objectives, except for observations of the O and Ne interstellar gas flow. The TOF efficiencies for H ENAs and the sputtered H component from the neutral interstellar He flow are reduced by about a factor of two, and the background is slightly elevated, but these changes do not impact the ENA observations significantly. In other words, IBEX-Lo still takes very clean observations.

6.3 Heliospheric Low Energy ENA Observations

The excellent noise and background suppression, good mass resolution, and large collecting power of IBEX-Lo has made several important heliospheric discoveries possible. During the implementation phase of IBEX it was not evident whether the H ISN flow would be detectable at 1 AU because of its very high ionization losses and the generally higher background susceptibility at the low H energies of 10 – 30 eV. Following the discovery of the He ISN flow with Ulysses GAS [Witte et al. 1996] and observations with IMAGE LENA [Collier et al. 2004], IBEX-Lo clearly identified the H ISN flow, along with the expected He and O ISN signal [Möbius et al. 2009]. For the first time, the effect of solar radiation pressure on the H ISN flow could be deduced quantitatively from direct particle observations [Schwadron et al., 2013].

By comparing the observed ratio of sputtered C and converted O in the O ISN flow signal with calibration results using an O and a Ne beam it was even possible to identify a Ne component in the ISN flow and to determine the Ne/O ratio of the interstellar gas outside the solar system [Bochsler et al., 2012; Park et al., 2014]. The resulting ratio for the pristine interstellar medium agrees with findings from pickup ion observations by Gloeckler and Geiss [1998], but these values suggest a higher Ne/O ratio than found in the solar system. This raises the question whether there are genuinely different abundances in the solar system compared with the local neighborhood or whether a substantial amount O may be locked in interstellar dust.

Most recently, IBEX-Lo has revealed secondary ISN flow components for O [Möbius et al., 2009; Park et al., 2015] and He [Kubiak et al., 2014]. These are thought to arise from charge

exchange between the diverted interstellar plasma in the outer heliosheath and the neutral interstellar flow. Such a component was predicted for O, but thought to be very weak for He [Müller & Zank 2004]. Their characteristics will shed light on the interaction process in the outer heliosheath and on the plasma diversion caused by the interstellar magnetic field.

7. Conclusions and Outlook

TOF spectrographs for space applications have come a long way since their first use on satellites in the mid 1980's. They can be adapted to a variety of uses and parameter ranges by combining several different building blocks and optimizing them based on prior experience and new needs. The inclusion of novel technologies, such as the potential replacement of C-foils by a single-stage MCP to achieve better TOF resolution, advanced ESA concepts to improve the effective geometric factor and duty cycle, as well as the use of modern solid state detector concepts to combine timing and energy measurement, ensures that the reach of TOF instrumentation will go even further. Large-scale integration technologies reduce the resource requirements of the electronics, and modern processor technologies help to optimize the data stream and to further reduce resources so that the electronics for TOF instruments can be reduced in size. The actual sensors are scaled based on the required collection capability, the required TOF path length, and high voltage constraints, so these aspects are much harder to miniaturize. TOF instruments have a wide range of applications from ionospheric and magnetospheric physics, via solar, interplanetary and interstellar physics to planetary applications.

With their tremendous achievements in the IBEX mission, TOF spectrographs also have paved the way to a more ambitious follow-on mission, the Interstellar Mapping and Acceleration Probe (IMAP). This mission, when implemented, will bring the ENA mapping of the heliosphere boundary and the sampling of the interstellar gas flow to the next level of resolution and collecting power. It will combine this capability with the crucial pickup ion diagnostics of the interstellar gas population and high cadence observations of suprathermal and energetic particles to trace their acceleration from the parent population to high energies. IMAP has been promoted as the highest priority for solar terrestrial probes in the recent Heliophysics Decadal Survey [Baker et al. 2013]. The scientific objectives of this mission depend crucially on a complement of TOF spectrographs, which are optimized for neutral atoms over an extended energy range compared with IBEX and for ions from pickup ion energies to about 1 MeV/nuc. The ENA TOF spectrographs can be optimized based on ample test, calibration, and flight experience with IBEX and CASSINI, and the PUI and suprathermal sensor will be the first dedicated instrument for this purpose based on ample experience from Ulysses, ACE, and STEREO. Without the advances made over the past 30 years in TOF technology and supporting sensor modules such mission would not be possible.

Acknowledgements: This work was partially supported by the IBEX Mission under Contract#NNG05EC85C, the STEREO Mission under Grant #NNX13AP52G, and an instrument development Grant #NNX12AH45G. The authors are grateful to their collaborators, engineers, project managers and administrative support people, who have made these efforts a success. Data used in this paper (data behind Figure 6 and 9) can be obtained from E. Möbius (eberhard.moebius@unh.edu).

References

Aellig, M. R., et al., (1998), Iron freeze-in temperatures measured by SOHO/CELIAS/CTOF, *J. Geophys. Res.*, **103**, 17215, doi: 10.1029/98JA00588.

Allegrini, F., et al., (2009), The entrance system laboratory prototype for an advanced mass and ionic charge composition experiment, *Rev. Sci. Instr.*, **80**, 104502, doi: 10.1063/1.4873327.

Allegrini, F., et al. (2016), A comprehensive suprathermal ion sensor suite, *this volume*.

Andrews, B., et al., (2007), The Energetic Particle and Plasma Spectrometer Instrument on the MESSENGER Spacecraft, *Space Sci. Rev.*, **131**, 523, doi:10.1007/s11214-007-9272-5.

Baker, D.N., et al., (2013), Solar and Space Physics, a Science for a Technological Society, The National Academies Press, Washington, D.C., ISBN 978-0-309-16428-3.

Balsiger, H., et al., (2007), Rosina Rosetta Orbiter Spectrometer for Ion and Neutral Analysis, *Space Sci. Rev*., **128**, 745-801, doi: 10.1007/s11214-006-8335-3.

Barabash, S., et al. (2006), The Analyzer of Space Plasmas and Energetic Atoms (ASPERA-3) for the Mars Express Mission, *Space Sci. Rev*., **126**, 113, doi: 10.1007/s11214-006-9124-8.

Barabash, S., et al. (2009), Investigation of the solar wind–Moon interaction onboard Chandrayaan-1 mission with the SARA experiment, Curr. Sci., 96, 526.

Blush, L.M., F. et al., (2005), Development and calibration of major components for the STEREO/PLASTIC (plasma and suprathermal ion composition) instrument, *Adv. Space Res*. **36**, 1556, doi: 10.1016/j.asr.2005.07.028.

Bochsler, P., et al., (1997), Limits of the efficiency of isotope fractionation processes in the solar wind derived from the magnesium isotopic composition as observed with the WIND/MASS experiment, *Phys. Chem. Earth*, **22**, 401.

Bochsler, P., et al., (2012), Estimation of the neon/oxygen abundance ratio at the heliospheric termination shock and in the local interstellar medium from IBEX observations, *Astrophys. J. Suppl*., **198**:13, doi:10.1088/0067-0049/198/2/13.

Bodmer, R., & P. Bochsler (1998), The helium isotopic ratio in the solar wind and ion fractionation in the corona by inefficient Coulomb drag, *Astron. Astrophys*., **337**, 921.

Bryant, D.A., S.M. Krimigis, & G. Haerendel (1985), Outline of the Active Magnetospheric Tracer Explorers (AMPTE) Mission, *IEEE Trans. on Geosci. El*., **GE-23**, 177.

Bzowski, M., J.M. et al., (2013), Solar Parameters for Modeling the Interplanetary Background, In: Cross-Calibration of Far UV Spectra of Solar System Objects and the Heliosphere, *ISSI Scientific Report Series*, **13**, 67, Springer, New York.

Cadu et al. (2016), Grazing incidence time-of-flight mass spectrometer: prototype results and possible improvements, *this volume*.

Chen, J., et al., (2013), Observational Study of the Cooling Behavior of Interstellar Helium Pick Up Ions in the Inner Heliosphere, *J. Geophys. Res*., **118**, 1, doi:10.1002/jgra.50391.

Collier, M. R., et al. (2004), An unexplained 10-40 degree shift in the location of some diverse neutral atom data at 1 AU, *Adv. Space Res.,* **34**, 166, doi: 10.1016/j.asr.2003.03.068.

Coplan, M.A., K.W. Ogilvie, P.A. Bochsler, & J. Geiss (1978), Ion Composition Experiment, *IEEE Trans. Geosci. El.*, **GE-16**, 185.

Czechowski, A., K. C., Hsieh, M. Hilchenbach, J. Kota, & A. W. Shaw (2004), Anomalous helium ions as the source of energetic helium atoms in the outer heliosphere, *Adv. Space Res.*, **34**, 104, doi: 10.1016/j.asr.2003.03.054.

Desai, M.I., G.M. et al., (2006), Heavy-Ion Elemental Abundances in Large Solar Energetic Particle Events and Their Implications for the Seed Population, *Astrophys. J.*, **649**, 470, doi: 10.1086/505649.

Desai, M. I., et al., (2015), An integrated time-of-flight versus residual energy subsystem for a compact dual ion composition experiment for space plasmas, *Rev. Sci. Instr.*, **86**, 054501, doi: 10.1063/1.4921706.

Desai, M., et al. (2016), Compact Dual Ion Composition Experiment for Space Plasmas – CoDICE, *this volume*.

Devoto, P., J.-L. Medale, J.-A. Sauvaud, J. Rouzaud, & C. Aoustin (2008), A mass spectrometer for investigations of the ion populations of the planetary environments using a new distributed grazing incidence technique, 37th COSPAR Sci. Assembly Montréal, Canada, p.707, Paper number: C32-0051-08.

Drews, C., et al., (2015), 2D He^+ pickup ion velocity distribution functions: STEREO PLASTIC observations, *Astron. & Astrophys.*, **575**, A97, doi:10.1051/0004-6361/201425271.

Funsten, H.F., B.L. Barraclough, & D.J. McComas (1994), Interactions of slow H, H_2, and H_3 with thin carbon foils, *Nucl. Instr. Meth. B*, **90**, 24, doi: 10.1016/0168-583X(94)95503-4.

Funsten, H.O., et al., (2009), The Interstellar Boundary Explorer High Energy (IBEX-Hi) Neutral Atom Imager, *Space Sci. Rev.*, **146**, 75, doi: 10.1007/s11214-009-9504-y.

Fuselier, S. A., et al., (2009), IBEX-Lo Sensor, *Space Sci. Rev.*, **146**, 117, doi: 10.1007/s11214-009-9495-8.

Funsten, H. F. (2016), Particle Measurements in Challenging Environments, *this volume*.

Galvin, A.B., L. et al., (2008), The Plasma and Suprathermal Ion Composition (Plastic) Investigation on the STEREO Observatories, *Space Sci. Rev.*, **136**, 437, doi: 10.1007/s11214-007-9296-x.

Galvin, A.B., K.D.C. Simunac, L.K. Jian, C.J. Farrugia, & M.A. Popecki (2013), Solar wind ion observations: comparison from the depths of solar minimum to the rising of the cycle, In: Proc. of the 13th Int. Solar Wind Conf., *AIP Conf. Proc.*, **1539**, 15, doi: 10.1063/1.4810978.

Geiss, J., F. Bühler, H. Cerutti, P. Eberhardt, & C. Filleux (1972), Solar wind composition experiment, in Apollo 16 Prelim. Sci. Rep., pp. 14.1-14.10, NASA SP-315.

Geiss, J., & H. Reeves (1972), Cosmic and Solar System Abundances of Deuterium and Helium-3, *Astron. Astrophys.*, **18**, 126.

Gilbert, J., et al. (2016), The Pickup Ion Composition Spectrometer, *this volume*.

Gloeckler, G., & K.-C. Hsieh (1979), Time-of-Flight Technique for Particle Identification of Energies from 2 to 400 keV/nucleon, *Nucl. Instr. Meth.*, **165**, 537.

Gloeckler, G., et al., (1985), The Charge-Energy-Mass Spectrometer for 0.3-300 keV/e Ions on the AMPTE CCE, *IEEE Trans. on Geosci. El.*, **GE-23**, 234.

Gloeckler, G. (1990), Ion composition measurement techniques for space plasmas, *Rev, Sci. Instr.*, **61**, 3613, doi: 10.1063/1.1141708.

Gloeckler, G., et al., (1992), The Solar Wind Ion Composition Spectrometer, *Astron. Astrophys. Suppl. Ser.*, **92**, 267.

Gloeckler, G., et al., (1995), The Solar Wind and Suprathermal Ion Composition Investigation on the WIND Spacecraft, *Space Sci. Rev.*, **71**, 79, doi: 10.1007/BF00751327.

Gloeckler, G., et al., (1998), Investigation of the composition of solar and interstellar matter using solar wind and pickup ion measurements with SWICS and SWIMS on the ACE spacecraft, *Space Sci. Rev.*, **86**, 497, doi: 10.1023/A:1005036131689.

Gloeckler, G., & J. Geiss (1998), Interstellar and Inner Source Pickup Ions Observed with SWICS on ULYSSES, *Space Sci. Rev.*, **86**, 127, doi: 10.1023/A:1005019628054.

Gloeckler, G., et al., (2004), Observations of the Helium Focusing Cone with Pickup Ions, *Astron. Astrophys.*, **426**, 845, doi: 10.1051/0004-6361:20035768.

Gonin, M., Buergi, A., Oetliker, M., & Bochsler, P. (1992), Interaction of solar wind ions with thin carbon foils: Calibration of time-of-flight spectrometers, *Proc. of the First SOHO Workshop: Coronal Streamers, Coronal Loops, and Coronal and Solar Wind Composition, ESA-SP*, pp. 381-384.

Gubler, L., P. Wurz, P. Bochsler, & E. Möbius (1995), High Resolution Isochronous Mass Spectrometer for Space Plasma Applications, *Int. J. Mass Spectr. and Ion Proc.,* **148**, 77.

Haerendel G., A. et al., (1985), The Li/Ba Release Experiments of the Ion Release Module, *IEEE Trans. on Geosci. El.*, **GE-23**, 253.

Hovestadt, D., & O. Vollmer (1971), A Satellite Experiment for Detecting Low Energy Heavy Cosmic Rays, *Proc. 12th Int. Cosmic Ray Conf.*, **4**., 1608.

Hovestadt, D., et al., (1978), The nuclear and ionic charge distribution particle experiments on the ISEE-1 and ISEE-C spacecraft, *IEEE Trans. on Geosci. El.*, **GE-16**, 166.

Hilchenbach, M., et al., (1998), Detection of 55 - 80 keV Hydrogen Atoms of Heliospheric Origin by CELIAS/HSTOF on SOHO, *Astrophys. J.*, **503**, 916, doi: 10.1086/306022.

Hovestadt, D., et al., (1995), CELIAS - Charge, Element and Isotope Analysis System for SOHO, *Sol. Phys.*, **162**, 441, doi: 10.1007/BF00733436.

Kallenbach, R., et al., (1997), Isotopic Composition of Solar Wind Neon Measured by CELIAS/MTOF onboard SOHO, *J. Geophys. Res.*, **102**, 26895, doi: 10.1029/97JA02325.

Kallenbach, R., et al., (1998), Fractionation of Si, Ne, and Mg isotopes in the solar wind as measured by SOHO/CELIAS/MTOF, *Space Sci. Rev.*, **85**, 357, doi: 10.1086/311702.

Kistler, L.M., et al., (2002), Motion of auroral ion outflow structures observed with CLUSTER and IMAGE FUV, *J. Geophys. Res.*, **107**, doi: 101029/2001JA005075.

Kistler, L.M., C. Mouikis, B. Klecker, & I. Dandouras (2010), The cusp as a source for oxygen in the plasma sheet during geomagnetic storms, *J. Geophys. Res*., **115**, A03209, doi: 10.1029/2009JA014838.

Klecker, E., et al., (1986), Discovery of energetic molecular ions (NO^+ and O_2^+) in the storm time ring current, *Geophys. Res. Lett*., **13**, 632, doi: 10.1029/GL013i007p00632.

Klumpar, D.M., et al., (2001), The Time-of-Flight Energy, Angle, Mass Spectrograph (TEAMS) Experiment for FAST, *Space Sci. Rev.*, **98**, 197, doi: 10.1023/A:1013127607414.

Krimigis, S.M., et al., (2004), Magnetosphere Imaging Instrument (MIMI) on the Cassini Mission to Saturn/Titan, *Space Sci. Rev*., **114**, 233, doi: 10.1007/s11214-004-1410-8.

Krimigis, S. M., D. G. Mitchell, E. C. Roelof, K. C. Hsieh, & D. J. McComas (2009), Imaging the Interaction of the Heliosphere with the Interstellar Medium from Saturn with Cassini, *Science*, **326**, 971, doi: 10.1126/science.1181079.

Kubiak, M. A., et al., (2014), Warm Breeze from the starboard bow: a new population of neutral helium in the heliosphere, *Astrophys. J. Suppl*., **213**:29, doi: 10.1051/0004-6361/201321166.

Kucharek, H., et al., (1998), Magnesium isotopic composition as observed with the CELIAS/MTOF experiment on the SOHO spacecraft, *J. Geophys. Res.*, **103**, 26805, doi: 10.1029/98JA02542.

Kucharek, H., et al., (2015), Impact of Planetary Gravitation on High Precision Neutral Atom Measurements, *Astrophys. J. Suppl*., **220**:35, doi:10.1088/0067-0049/220/2/35.

Lepri, S.T., et al., (2001), Iron Charge Distributions as an Identifier of Interplanetary Coronal Mass Ejections, *J. Geophys. Res.,***106**, 29231, doi: 10.1029/2001JA000014.

Liu, Y. H., et al., (2015), The heavy ion diffusion region in magnetic reconnection in the Earth's magnetotail, *J.Geophys. Res.*, **120**, 3535, doi: 10.1002/2015JA020982.

Livi, S., E. Möbius, D. Haggerty, M. Witte, & P. Wurz, (2003), An Interstellar Neutral Atom Detector, *AIP Conf. Proc*., **679**, 850, doi: 10.1063/1.1618724.

Livi, S. (2016), STROFIO: A Novel Neutral Mass Spectrograph for Sampling Mercury's Exosphere Rams: A Miniature Ram Angle and Magnetic Field Sensor, *this volume*.

Lund, E J, et al., (1998), FAST observations of preferentially accelerated He^+ in association with auroral electromagnetic ion cyclotron waves, *Geophys. Res. Lett*., **25**, 2049, doi: 10.1029/98GL00304.

Managadze, G.G. (1986), Time-of-flight Ion Mass Analyzer, *U.S. Patent* Number 4, 611, 118.

Marti, K., & P. Bochsler (2012), Solar Wind and Solar System Matter After Mission Genesis, In: Exploring the solar wind, Ch. 4, DOI: 10.5772/36974, M. Lazar, ed., InTech, ISBN: 978-953-51-0399-4.

Mason, G. M., et al., (1990), SAMPEX Mission Overview, *AIP Conf. Proc*., **203**, 44, doi: 10.1063/1.39140.

Mason, G. M., et al., (1993), LEICA: A Low Energy Ion Composition Analyzer for the Study of Solar and Magnetospheric Heavy Ions, *IEEE Trans. on Geosci. Rem. Sens.*, **31**, 549.

Mason, G. M., et al., (1998), The Ultra-Low-Energy Isotope Spectrometer (ULEIS) for the ACE spacecraft, *Space Sci. Rev*., **86**, 409, doi: 10.1023/A:1005079930780.

Mason, G. M., Desai, M. I., Mazur, J. E., & Dwyer, J. R. (2005), Energetic Particles Accelerated by Shocks in the Heliosphere: What is the Source Material? In: The Physics of Collisionless Shocks: *AIP Conf. Proc*., **781**, 219, doi: 10.1063/1.2032700.

Mason, G. M., et al., (2008), The Suprathermal Ion Telescope (SIT) For the IMPACT/SEP Investigation, *Space Sci. Rev*., **136**, 257, doi: 10.1007/s11214-006-9087-9.

McComas, D.J., J.E. Nordholt, J.-J. Berthelier, J.-M. Illiano, & D.T. Young (1998), The Cassini Ion Mass Spectrometer, In: Measurement Techniques in Space Plasmas, R. Pfaff, J. Borowski, D. Young eds., *Geophys. Monogr.* **102**, 187.

McComas, D.J., et al., (2004), Ultrathin (≈10 nm) carbon foils in space instrumentation, *Rev. Sci. Instr*., **75**, 4863, doi: 10.1063/1.1809265.

McComas, D.J., et al., (2009a), IBEX - Interstellar Boundary Explorer, *Space Sci. Rev*., **146**, 11, doi: 10.1007/s11214-009-9499-4.

McComas, D. J., et al., (2009b), Global Observations of the Interstellar Interaction from the Interstellar Boundary Explorer (IBEX), *Science*, **326**, 959, doi: 10.1126/science.1180906.

McEntire, R. W., E. P. Keath, D. E. Fort, A. T. Y. Lui, & S. M. Krimigis (1985), The Medium-energy particle analyzer (MEPA) on the AMPTE CCE spacecraft, *IEEE Trans. on Geosci. El*., **GE-23**, 230.

McFadden, J.M. (2016), Technology Challenges for Space Plasma Measurements, *this volume*.

Mitchell, D. G., et al., (1996), Imaging-neutral camera (INCA) for the NASA Cassini mission to Saturn and Titan, *Proc. SPIE*, **2803**, 154.

Mitchell, D. G., et al., (2000), The High-Energy Neutral Atom (HENA) Imager for the IMAGE mission, *Space Sci. Rev*., **91**, 67, doi: 10.1023/A:1005207308094.

Mitchell, D.G., et al., (2001), Imaging Two Geomagnetic Storms in Energetic Neutral Atoms. *Geophys Res. Lett*., **28**, 1151, doi: 10.1029/2000GL012395.

Möbius, E., et al., (1985a), The time-of-flight spectrometer SULEICA for ions of the energy range 5-270 keV/charge on the AMPTE/IRM, *IEEE Trans. on Geosci. El*., **GE-23**, 274.

Möbius, E., et al., (1985b), Direct observation of He^+ pick-up ions of interstellar origin in the solar wind, *Nature*, **318**, 426, doi: 10.1038/318426a0.

Möbius, E., et al., (1986), Observation of lithium pick-up ions in the 5 to 20 keV energy range following the AMPTE solar wind releases, *J. Geophys. Res*., **91**, 1325, doi: 10.1029/JA091iA02p01325.

Möbius, E., P. Bochsler, A.G. Ghielmetti, & D.C. Hamilton (1990), High mass resolution isochronous Time-of-flight spectrograph for three-dimensional space plasma measurements, *Rev. Sci. Instr.*, **61**, 3609, doi: 10.1063/1.1141580.

Möbius, E., et al., (1998a), The 3-D Plasma Distribution Function Analyzers With Time-of-Flight Mass Discrimination for CLUSTER, FAST and Equator-S, In: Measurement Techniques in Space Plasmas, R. Pfaff, J. Borowski, D. Young eds., *Geophys. Monogr.* **102**, 243.

Möbius, E, et al., (1998b), Species dependent energies in upward directed ion beams over auroral arcs as observed with FAST TEAMS, *Geophys. Res. Lett.*, **25**, 2029, doi: 10.1029/98GL00381.

Möbius, E., et al., (2008), Time-of-Flight Detector System of the IBEX-Lo Sensor with Low Background Performance for Heliospheric ENA Detection, *Proc. of the 30th Int. Cosmic Ray Conf.*, **Vol. 1**, 841-844, Universidad Nacional Autónoma de México, Mexico.

Möbius, E., et al., (2009), Direct Observations of Interstellar H, He, and O by the Interstellar Boundary Explorer, *Science*, **326**, 969, doi: 10.1126/science.1180971.

Moore, T. E., et al., (2000), The Low-Energy Neutral Atom (LENA) Imager Investigation, *Space Sci. Rev.*, **91**, 155, doi: 10.1023/A:1005211509003.

Mouikis, C. G., et al., (2002), Equator-S observations of He^+ energization by EMIC waves in the dawnside equatorial magnetosphere, *Geophys. Res. Lett.*, **29**, 74, doi: 10.1029/2001GL013899.

Müller, H.-R., & G. P. Zank (2004), Heliospheric filtration of interstellar heavy atoms: Sensitivity to hydrogen background, *J. Geophys. Res.*, **109**, A07104, doi: 10.1029/2003JA010269.

Ogasawara, K., et al., (2015), Single crystal chemical vapor deposit diamond detector for energetic plasma measurement in space, *Nucl. Instr. Meth. A*, **777**, 131, doi:10.1016/j.nima.2014.12.098.

Orsini, S., et al., (2010), SERENA: A suite of four instruments (ELENA, STROFIO, PICAM and MIPA) on board BepiColombo-MPO for particle detection in the Hermean environment, *Planet. Space Sci.*, **58**, 166, doi:10.1016/j.pss.2008.09.012.

Park, J., et al., (2014), The Ne to O abundance ratio of the interstellar medium from the IBEX-Lo observations, *Astrophys. J.*, **795**:97, .

Park, J., et al., (2015), Statistical analysis of the heavy neutral atoms measured by IBEX, *Astrophys. J. Suppl.*, **220**:34, doi: 10.1088/0004-637X/795/1/97.

Paschalidis, N. (2016), Advanced gated time of flight mass spectrometers for Small Satellites and Cubesats, *this volume*.

Paschmann, G., et al., (1985), The Plasma Instrument for the AMPTE IRM, *IEEE Trans. on Geosci. El.*, **GE-23**, 262.

Pollock, C. J., et al., (2000), Medium Energy Neutral Atom (MENA) Imager for the IMAGE Mission, *Space Sci. Rev.*, **91**, 113, doi: 10.1023/A:1005259324933.

Rème, H., et al., (1997), The CLUSTER Ion Spectrometry Experiment, *Space Sci. Rev.*, **79**, 303, doi: 10.1023/A:1004929816409.

Schwadron, N.A., et al., (2013), Solar Radiation Pressure and Local Interstellar Medium Flow Parameters from Interstellar Boundary Explorer Low Energy Hydrogen Measurements, *Astrophys. J.*, **775**, 86, doi: 10.1088/0004-637X/775/2/86.

Shelley, E. G., et al., (1978), *IEEE Trans. on Geosci. El.*, **GE-16**, 266.

Skoug, R., et al., (2016), Wide Field-of-View Plasma Spectrometer, *this volume*.

von Steiger, R., et al., (2000), Composition of quasi-stationary solar wind flows from Ulysses/Solar Wind Ion Composition Spectrometer, *J. Geophys. Res*. **105**, 27217, doi: 10.1029/1999JA000358.

Wang, S., L. M. Kistler, C. G. Mouikis, & S. M. Petrinec (2015), Dependence of the dayside magnetopause reconnection rate on local conditions, *J. Geophys. Res*., **120**, 6386, doi: 10.1002/2015JA021524.

Wimmer-Schweingruber, R.F., et al., (1999), On the bulk isotopic composition of magnesium and silicon during the May 1998 CME: ACE/SWIMS, *Geophys. Res. Lett*., **26**, 165, doi: 10.1029/1999GL010676.

Wimmer-Schweingruber, R.F. (2002), The Composition of the Solar Wind, *Adv. Space Res*., **30**, 23, doi: 10.1016/S0273-1177(02)00262-4.

Winslow, R.M., et al., (2016), A perfect conjunction between Messenger and STEREO A: Development of ICME Complexity through Stream Interactions, *J. Geophys. Res*., subm.

Witte, M., Banaszkiewicz, M., & Rosenbauer, H., (1996), Recent results on the parameters of the interstellar helium from the ULYSSES/GAS experiment, *Space Sci. Rev*., **78**, 289, doi: 10.1007/BF00170815.

Wüest, M. (1998), Time-of-Flight Ion Composition Measurement Technique for Space Plasmas, in: *Measurement Techniques in Space Plasmas – Particles*, R. F. Pfaff, J. E. Borovsky and D. T. Young eds., *Geophys. Monograph* 102, p. 141.

Wurz, P., et al., (2009), IBEX Backgrounds and Signal to Noise Ratio, *Space Sci. Rev*., **146**, 173, doi:10.1007/s11214-009-9515-8.

Ziegler, J.F., J.P. Biersack, & M.D. Ziegler (2015), SCRIM – The Stopping and Range of Ions in Matter, 15th edition, Lulu Press Company.

Zurbuchen, T., et al. (2016), Innovations in Plasma Analyzers, *this volume*.